Supporting Information

Defect-less Formamidinium Sn-Pb Perovskite Grown on Fluorinated Substrate with Top-down Crystallization Control for Efficient and Stable Photovoltaics

Yuan Zhou,[a] Tonghui Guo,[a] Junjun Jin,[a] Zhenkun Zhu,[a] Yanyan Li,[b] Shuxin Wang,[b] Sisi Zhou,[c] Qianqian Lin,[b] Jinhua Li,[d] Weijun Ke,[b] Guojia, Fang,[b] Xianggong Zhang[c] and Qidong Tai*[a]*

[a] The Institute of Technological Sciences, Wuhan University, Wuhan 430072, P. R. China.

[b]School of Physics and Technology, Wuhan University, Wuhan 430072, P. R. China

[c]Wuhan Institute of Marine Electric Propulsion, Wuhan 430064, China

[d]School of Materials Science and Engineering, Hubei University, Wuhan, 430062, China

*Corresponding author.

Email addresses: qdtai@whu.edu.cn (Q. Tai), xianggongzhang@sohu.com (X. Zhang)

Experimental Section

Materials: Sn powder, lead iodide (PbI_2, ultra-dry, metals basis, 99.999%), SnF_2 and Bathocuproine (BCP, 96%) ordered from Alfa Aesar. SnI_2, methylammonium chloride (MACl), cesium iodide (CsI), methylammonium bromide (MABr), and phenyl-C_{61}-butyric acid methyl ester ($PC_{61}BM$, 99.9%) were obtained from Advanced Election Technology Co. Ltd. Formamidinium iodide ($NH_2CH{=}NH_2I$, FAI) was obtained from GreatCell Solar. Formylhydrazine and Trifluoroacetamide (TFOA) were purchased from Innochem. Dimethylsulfoxide (DMSO, anhydrous, 99.9%), N, N-dimethylformaide (DMF, anhydrous, 99.8%) and Chlorobenzene (CB, Spectrophotometric Grade, 99.9%) were all purchased from Sigma-Aldrich. All materials and solvents are commercially available without additional purification.

Solution preparation: NiO_x nanocrystals were dissolved into deionized water to prepare 7 mg/ml NiO_x solution. SnI_2, FAI and SnF_2 in the 1.65:1.65:0.165 molar stoichiometric ratio with the appropriate amount of tin powder were dissoved into the DMF/DMSO mixed solvent for preparing the 1.65 M $FASnI_3$ precursor solution. PbI_2, FAI, MACl, MABr and CsI in a 1.65:1.4:0.3:0.2:0.1 molar stoichiometric ratio were dissoved into the DMF/DMSO mixed solvent for preparing the 1.65 M $FAPbI_3$ precursor solution. The mixed solvent ratio of DMF and DMSO is 1: 4. The $FAPb_{0.5}Sn_{0.5}I_3$ perovskite solution was obtained by stirring 1:1 ratio of $FASnI_3$ and $FAPbI_3$ precursor solution overnight at room temperature.[1] 2 mg/ml TFOA/DMF solution was prepared by dissolving TFOA in DNF. 30 mg/ml $PC_{61}BM$ solution and 0.5 mg/ml BCP solutions was prepared by dissolving $PC_{61}BM$ and BCP into chlorobenzene and isopropyl alcohol, respectively. We filtered all the above solutions with a 0.22 um filter prior to use.

Device fabrication: The clean ITO-coated glass substrates were obtained by ultrasonic in deionized

(DI) water, ethanol, acetone, isopropyl alcohol and ethanol solutions for 15min. These dry glass substrates were then placed in a UV-Ozone instrument for 20 min. After spin-coating the NiO_x solution on ITO substrates at 4000 rpm for 30 s, it was annealed on a hotplate at 150 °C for 30 min under air environment. Subsequently, TFOA buffer layer was spin-coated on NiO_x/ITO substrate at 4000 rpm for 30 s in a N_2-filled glove box. Then 60 μl perovskite precursor solution was dripped onto the prepared substrate and spin-coated at the rate of 5000 rpm for 33 s, during which 200 ul CB antisolvent was glibly dripped onto the perovskite wetted substrate at 18 s from the start. Then the prefabricated film was annealed at 130° for 20min in formylhydrazine vapor (FHV) atmosphere to obtain the perovskite film. Next the $PC_{61}BM$/CB solution was spin-coated at 2000 rpm for 30 s and the BCP/IPA solution was spin-coated at 6000 rpm for 1 min. Finally, a layer of 200 nm silver (Ag) electrode was evaporated on top of the films in a thermal evaporator (PD400S, Wuhan PDVacuum). The active areas of the device were limited to be 0.06 cm^2 with a circular metal mask during electrode deposition.

Exfoliation Procedure: Firstly, the $FAPb_{0.5}Sn_{0.5}I_3$ perovskite films based on bare NiO_x and NiO_x/TFOA ITO glass substrates (1.5*1.5 cm^2) were prepared in N_2-filled glove box. Then prepare another two clean glass slides with the size of 1.5*4 cm^2, where the position of 1.5*1.5 cm^2 is covered withthe Ultraviolet curing adhesive, and one side of the two glass slides with curing adhesive are tightly bonded on one side of each perovskite film on ITO glass. Next the two glass slides are illuminated with an ultraviolet lamp for an hour to completely cure the UV adhesive. The perovskite films glued to the slides can be obtained by separating the glass slide and ITO glass. The bottom side of the perovskite film can be observed at this time.

Material and device characterization: The Keithley 2400 source under AM 1.5 G simulated irradiation (100 mW cm^{-2}) from a solar simulator (Newport 94023A) was used to measure the current density-

voltage *(J-V)* curves of perovskite solar cells. The Newport TLS130B-300X instrument measured the external quantum efficiency (EQE) curves under a specialized EQE setup. We performed the *J-V* and EQE measurement in an air environment without encapsulation and limited the effective area of the perovskite solar cells to be 0.06 cm^2 by a circular metal mask. The maximum-power-point-tracking (MPPT) stability test was carried out by irradiating the sample encapsulated with Ultraviolet curing adhesive under white light (100 mW cm^{-2}) without cooling in atmospheric environment (MPP Tracking – 4B). The bottom/top surface and cross-sectional SEM images of the perovskite films and EDS signal distribution of Pb, Sn, and I three elements were acquired on a field-emission scanning electron microscope (FE-SEM, Hitachi SU8010). The XRD and depth-dependent grazing incidence XRD (GIXRD) measurements were conducted on a Bruker D8 focus X-ray diffractometer with a Cu K_α resource. Fourier-transform infrared (FTIR) spectroscopy was obtained from a Nicolet iS50 FT-IR spectrometer (Thermo Scientific, USA) with a SMART iTR Diamond. Electroluminescent spectra (EL) measurement was performed using an external quantum efficiency (EQE) system (Enli Technology Co. Ltd.) at room temperature in a N_2-atmosphere glove box. The UV-*vis* datas were gained from a UV-2600 spectrophotometer (Shimadzu, Japan). The Thermo Fisher ESCALAB 250XL (USA) instrument was used to analysis X-ray photoelectron spectroscopy (XPS) and ultraviolet photoelectron spectroscopy (UPS) datas, and a −5 V bias was applied for UPS measurement. We used the FLS980 (Edinburgh Inc) instrument to measure the steady-state photoluminescence (PL) and time resolved photoluminescence (TRPL) decay. We tested the transient absorption spectra (TAS) through the femtosecond laser (Carbide, Light Conversion) and optical parametric amplifier (Orphrus-hp, Light Conversion), and we recorded it using a commercial spectrometer (HARPIA-TA, Light Conversion). Time-of-flight secondary ion mass spectrometry (ToF-SIMS) datas were collected by a TOFSIMS5

(ION-TOF GmbH, Germany) instrument. The AFM (Bruker Multimode 8) instrument was used to measure the surface roughness of films (NiO_x and perovskite) and analysis the KPFM of NiO_x films. All the characterizations of the samples were performed in ambient conditions at room temperature without encapsulation.

Calculation: The theoretical calculations were performed via the Gaussian 16 suite of programs.[2] The structure of the studied molecule was fully optimized at the PBE0-D3BJ/def2-SVP level of theory. The DFT-D3 with BJ-damping was applied to correct the weak interaction to improve the calculation accuracy. The vibrational frequencies of the optimized structures were carried out at the same level. The structures were characterized as a local energy minimum on the potential energy surface by verifying that all the vibrational frequencies were real. The singlet point energy calculations were performed with a larger basis set def2-TZVPD basis set. The dipole moment and the molecular electrostatic potential (MESP) of the molecule were calculated and analyzed. The Visual Molecular Dynamics (VMD) program [3] was used to plot the color-filled iso-surface graphs to visualize the MESP.

XPS fitting: The measured full peaks of Sn were firstly imported through *XPS Peak* software. After determining the Sn^{2+} and Sn^{4+} peaks position, the fitting was performed with the *Optimise All* option.

Bi-exponential function fitting: Both the kinetic decay trace of the TAS and the TRPL are fitted by the bi-exponential function: $y(t) = A_1e^{-t/\tau1} + A_2e^{-t/\tau2} + y_0$, where τ_1 and τ_2 are first- and second-order decay times, A_1 and A_2 represent weighting coefficients of each decay channel, y_0 is a constant. The average TA lifetime and the average carrier lifetime (τ_{ave}) are calculated according to the following equation $\tau_{ave} = A_1\tau_1\tau_1/(A_1\tau_1 + A_2\tau_2) + A_2\tau_2\tau_2/(A_1\tau_1+A_2\tau_2)$.[1]

The trap density values calculated from SCLC: The electron trap density (ŋ) is estimated by the trap-filled limit voltage (V_{TFL}) with the following equation $ŋ = 2V_{TFL}\varepsilon\varepsilon_0 / eL^2$, where ε_0 is the vacuum

permittivity (ε_0 =8.854 * 10^{-14} F/cm), ε is the relative dielectric constant of the perovskite (around 32). e is the charge of an electron (e = 1.6 * 10^{-19}), L is the thickness of perovskite thin film (≈ 570 nm).[4]

Supplementary figures and analysis

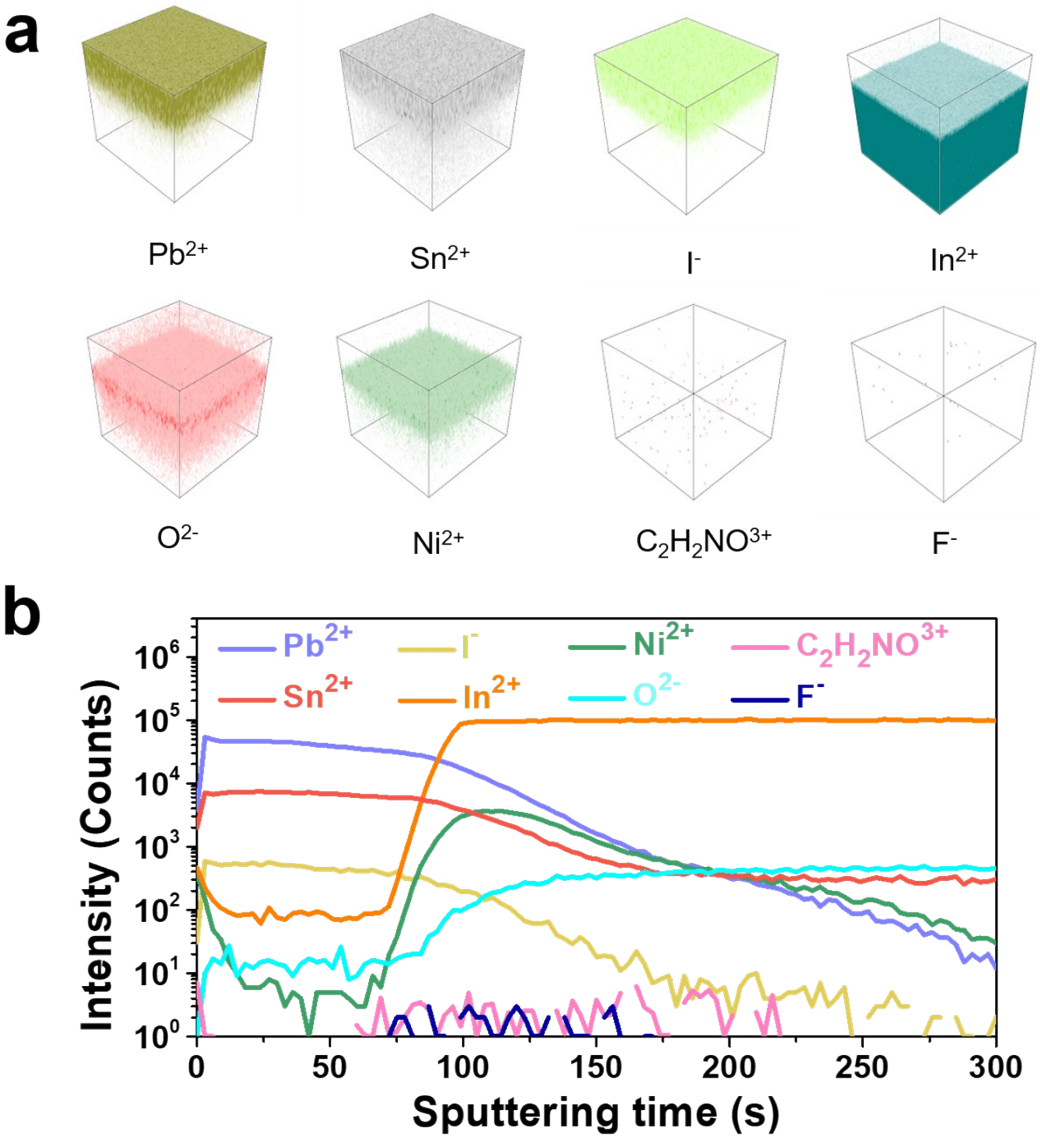

Fig. S1 Burying the TFOA buffer layer at the NiO_x/perovskite interface. (a) The spatial distribution and (b) the ToF-SIMS depth profile of different ions through the NiO_x and perovskite films.

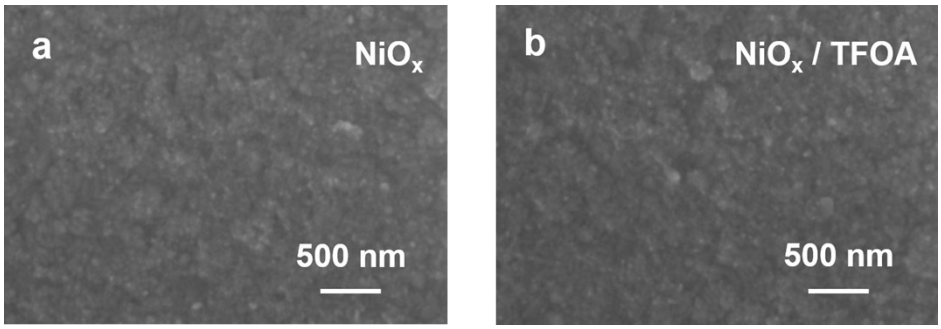

Fig. S2 SEM images of (a) bare NiO_x and (b) NiO_x/TFOA films.

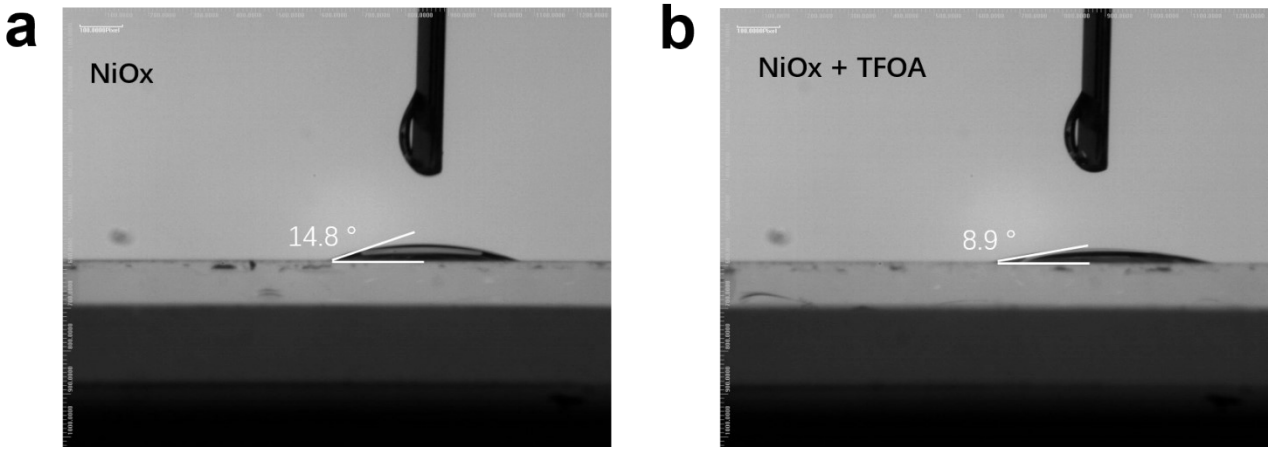

Fig. S3 The contact angle of perovskite solution on (a) bare NiO_x and (b) NiO_x/TFOA substrates.

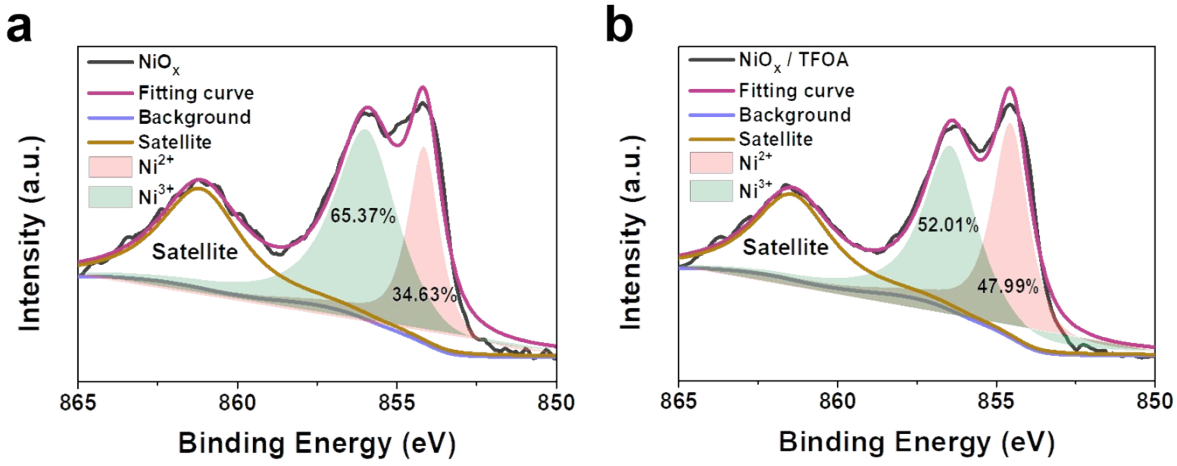

Fig. S4 Ni XPS spectra of (a) bare NiO_x and (b) NiO_x/TFOA films.

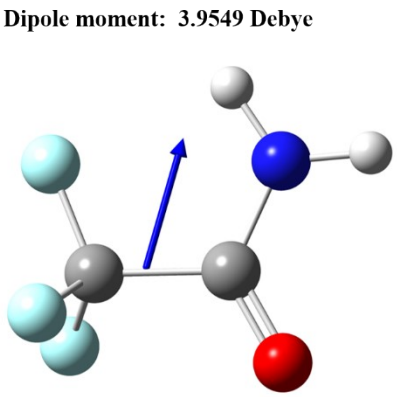

Fig. S5 Dipole moment of the TFOA molecular.

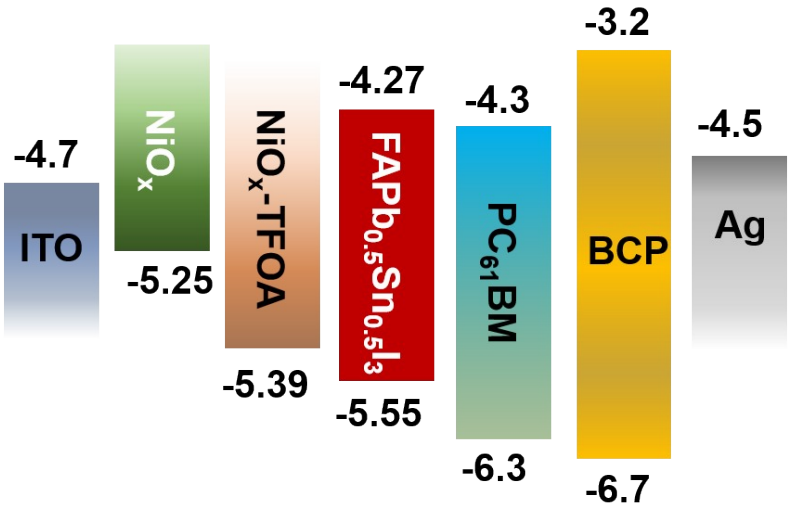

Fig. S6 Energy-level alignment diagram of the device with/without TFOA.

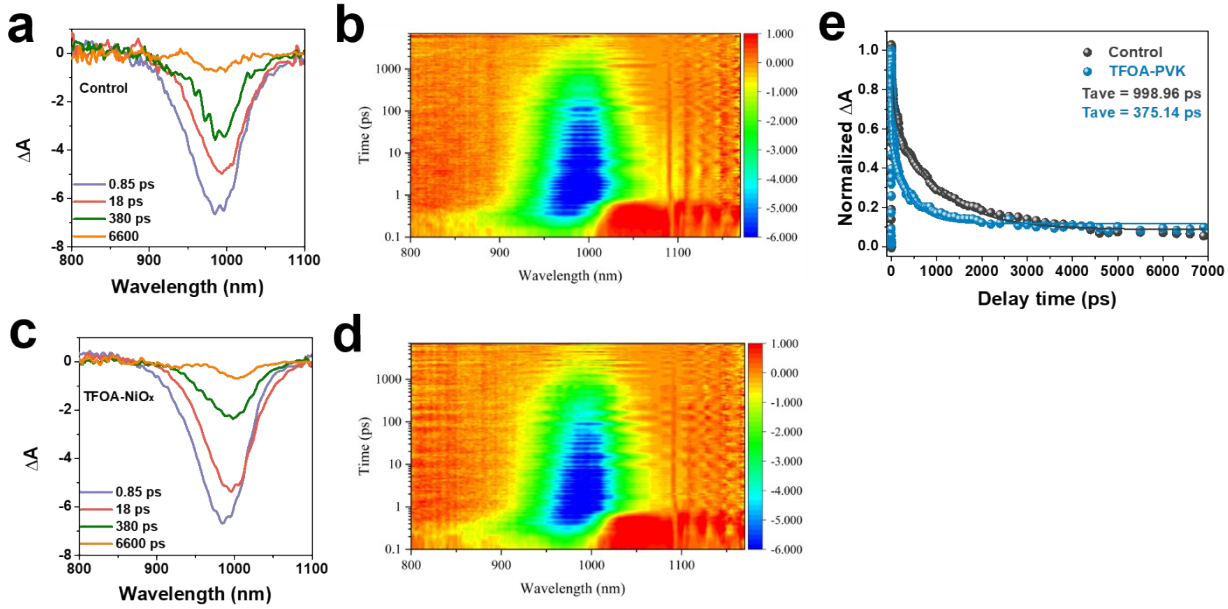

Fig. S7 The TA spectra excited from back side for $FAPb_{0.5}Sn_{0.5}I_3$ perovskite films based on (a) bare NiO_x and (c) NiO_x/TFOA substrates. (b) and (d) are the corresponding 2D color plots TA spectra. (e) Normalized transient band edge bleaching kinetics (990 nm) decay curves.

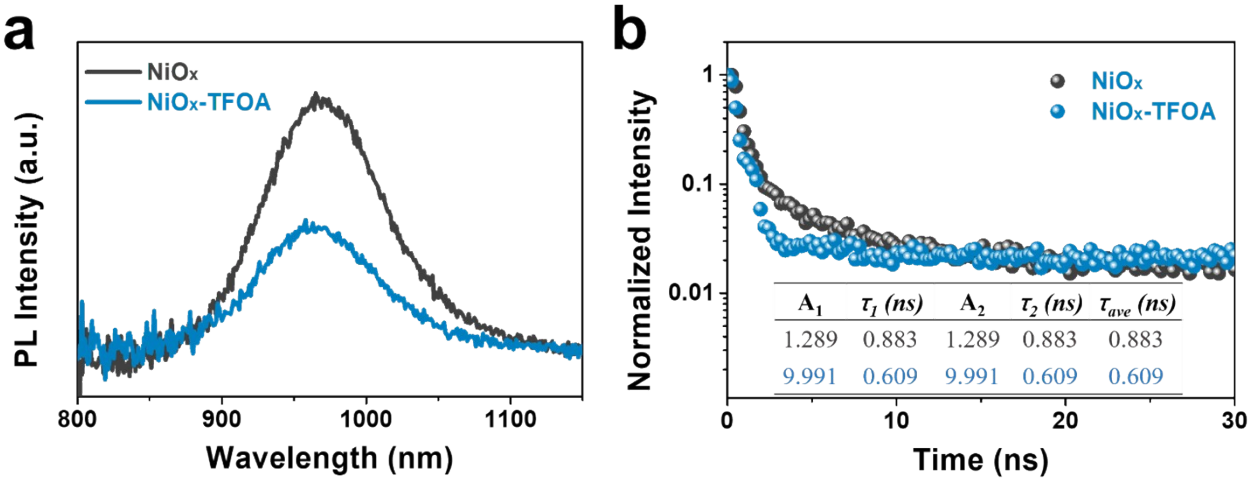

Fig. S8 (a) PL and (b) TRPL datas of perovskite films based on bare NiO_x and NiO_x/TFOA substrates.

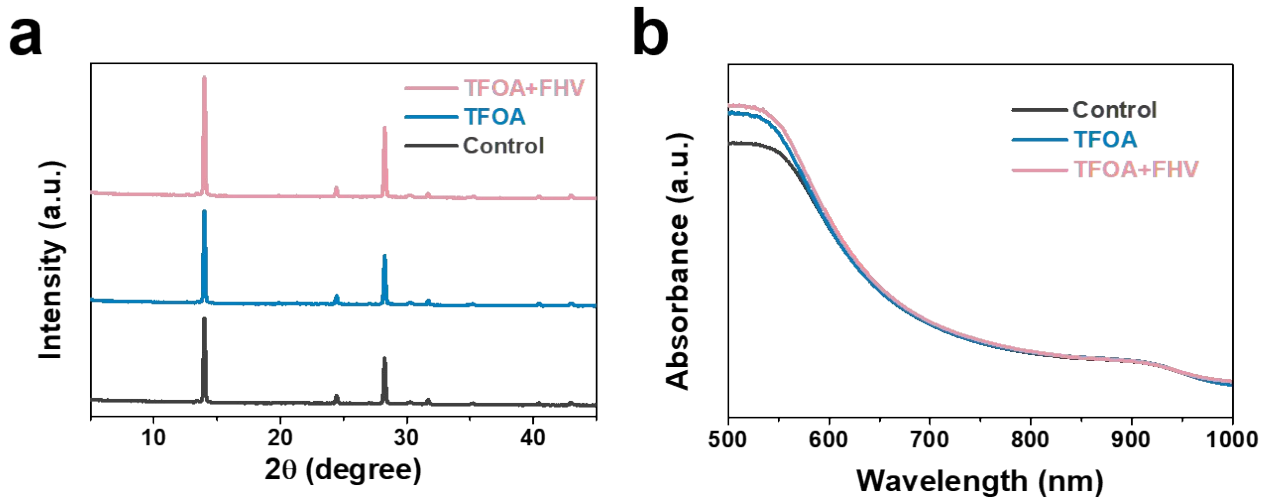

Fig. S9 (a) XRD characteristics and (b) UV-vis adsorption spectra of perovskite films under three conditions (Control, TFOA-only, and TFOA-FHV-based).

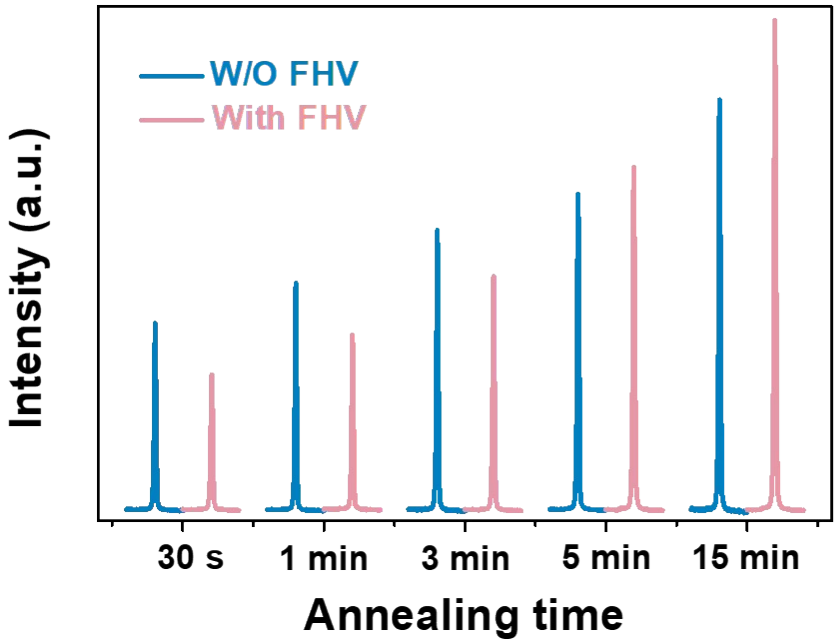

Fig. S10 The XRD characterization of two perovskite films with/without FHV at different annealing times. The FHV-treated perovskite films showed lower crystallinity in the first three minutes of annealing, which is due to the presence of formyl hydrazide inhibiting the crystallization and nucleation of the perovskite crystals, resulting in fewer nucleation sites. At five minutes of annealing, the crystallinity of FHV treated perovskite films was higher than that of untreated films, indicating that nucleation of perovskite crystals had been completed at this moment, and the crystals began to

gradually grow within 20 minutes of annealing and achieved full crystallization. Fewer nucleation sites could provide more space for the crystal to have greater growth potential, so FHV-treated perovskite films showed larger grains and higher crystallinity.

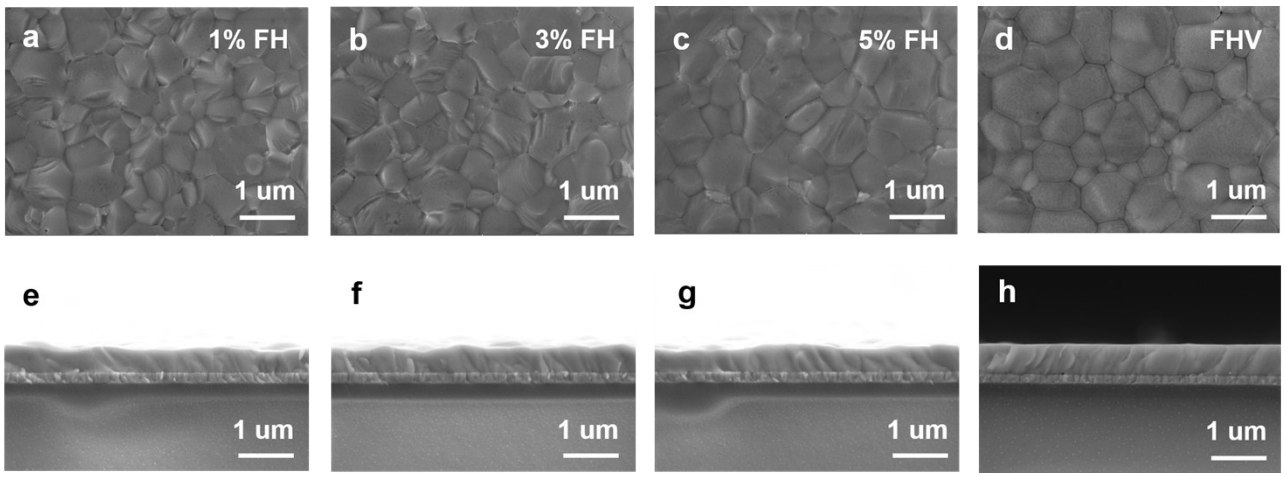

Fig. S11 The surface and corresponding cross-section SEM images of perovskite films under different conditions. In the absence of TFOA modification, (a-c,e-g) different formyl hydrazine content as additives and (d,h) formyl hydrazine vapor treatment.

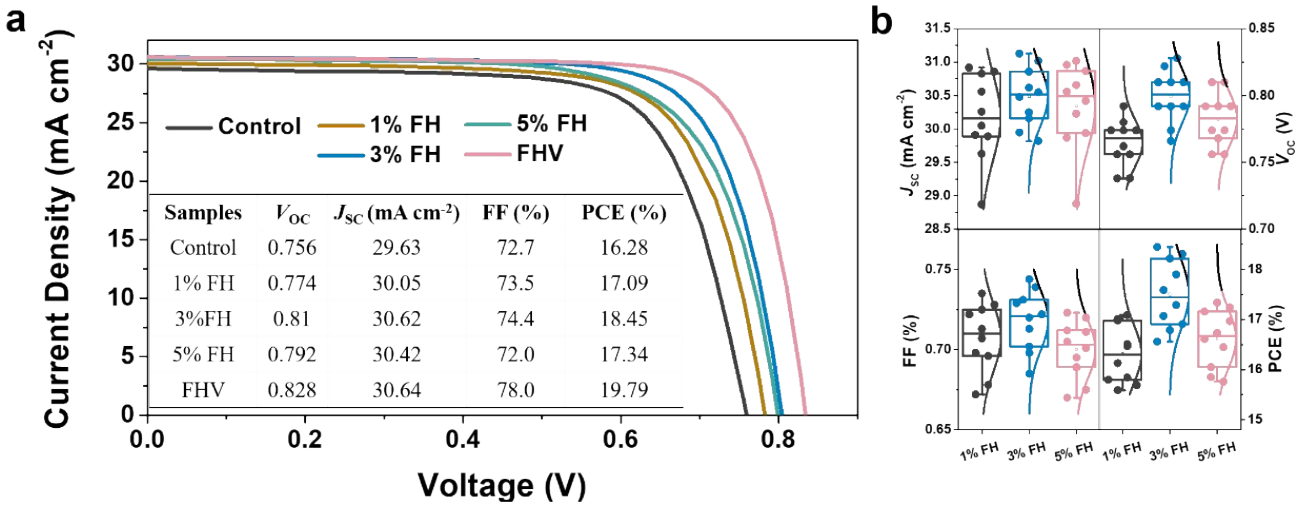

Samples	V_{OC}	J_{SC} (mA cm^{-2})	FF (%)	PCE (%)
Control	0.756	29.63	72.7	16.28
1% FH	0.774	30.05	73.5	17.09
3%FH	0.81	30.62	74.4	18.45
5% FH	0.792	30.42	72.0	17.34
FHV	0.828	30.64	78.0	19.79

Fig. S12 (a) The *J-V* curves of the best-performed control, 1% FH additive, 3% FH additive, 5% FH additive and FHV-treated devices in the absence of TFOA modification under reverse scan directions. (b) The distributions of J_{SC}, V_{OC}, FF and PCE for 10 devices under three conditions (1% FH additive, 3% FH additive and 5% FH additive).

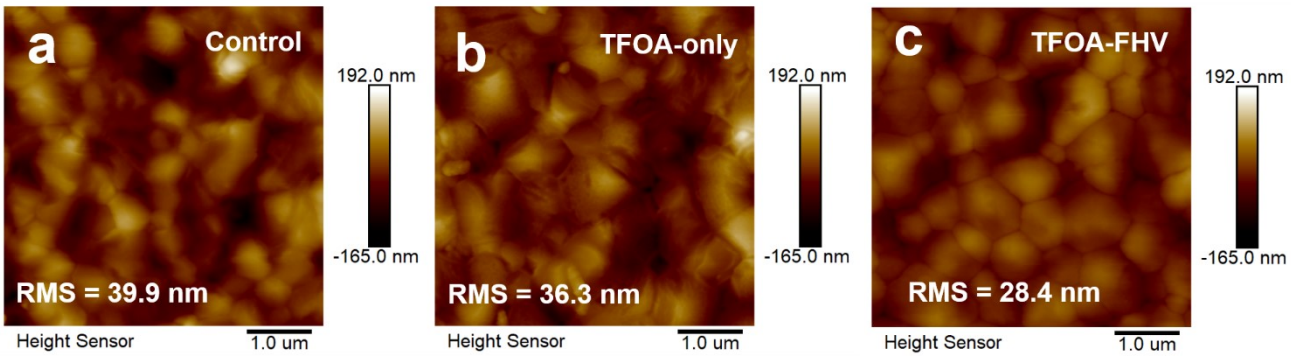

Fig. S13 AFM images of perovskite films under three conditions, (a) control, (b) TFOA-only, and (c) TFOA-FHV based.

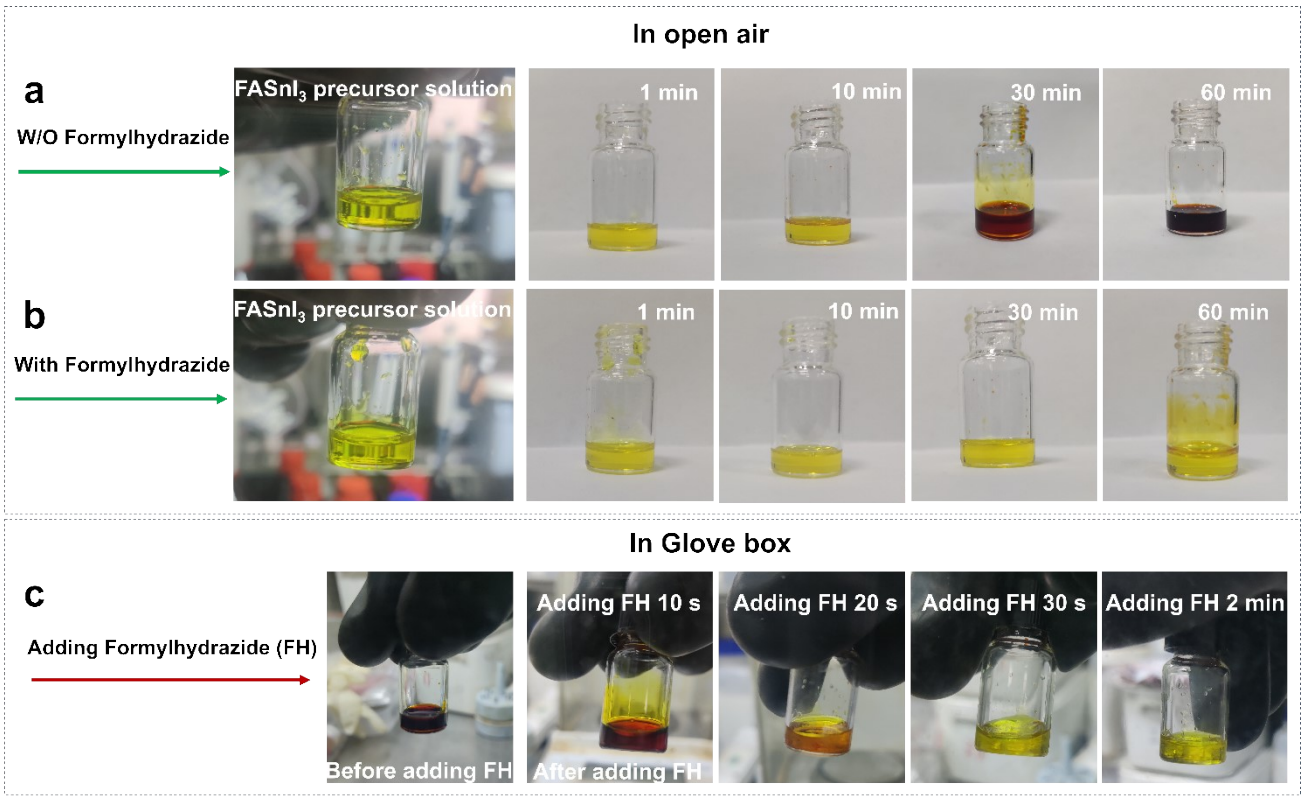

Fig. S14 The photographic images of $FASnI_3$ perovskite solution (a) without formylhydrazide and (b) with formylhydrazide in atmospheric environment for different periods of time (Sn^{2+} to Sn^{4+}). (c) The photographic images after adding formylhydrazide additive to the oxidized $FASnI_3$ precursor solution in the N_2-filled glove box for different periods of time (Sn^{4+} to Sn^{2+}).

As shown in Fig. S14, we firstly prepared two $FASnI_3$ perovskite precursor solutions (a) without and

(b) with formylhydrazide, and placed them in open air environment. From Fig. S14a, we can see that the original yellow color of the solution gradually changed to reddish-brown over time for the $FASnI_3$ precursor solution without formylhydrazide and finnally brownnish black after an hour (the oxidation of Sn^{2+} to Sn^{4+}), whereas this is not the case for the solution with formylhydrazide which still remains yellow after an hour (Fig. S14b). To further illustrate the reductibility of formylhydrazide, then we transferred the brownish black $FASnI_3$ perovskite precursor solution into a N_2-filled glove box and added excess formylhydrazide to shake well. As can be seen from Fig. S14c, the color of the solution rapidly changed to yellow after the additon of formylhydrazide with shaking, and was almost the same as the beginning yellow after 30 s (the reduction of Sn^{4+} to Sn^{2+}). These results indicated that formylhydrazide with hydroxyl functional group has excellent reducing properties and can be used as an antioxidant to prevent the oxidation of Sn^{2+} ions in Sn-based perovskite.

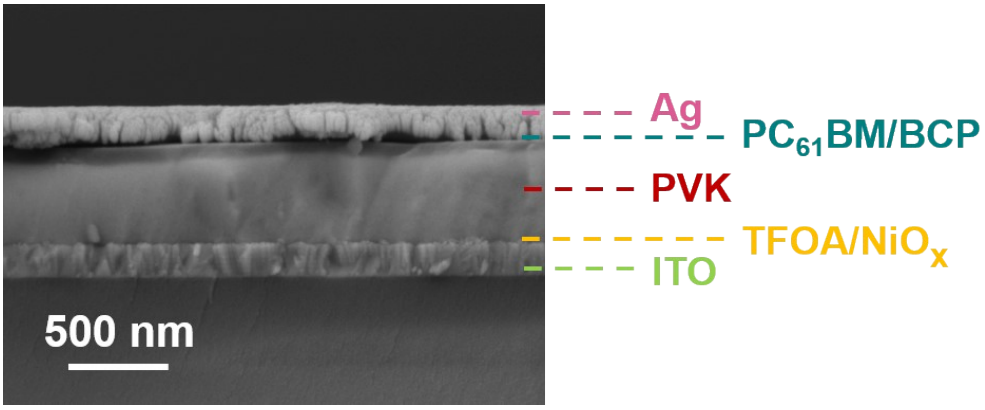

Fig. S15 The cross-sectional SEM image of the real device with TFOA buffer layer.

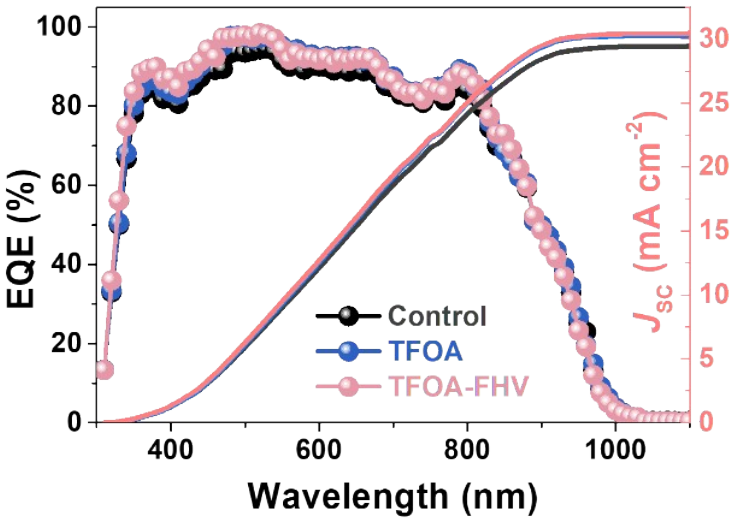

Fig. S16 EQE spectra and the corresponding integrated current density curves.

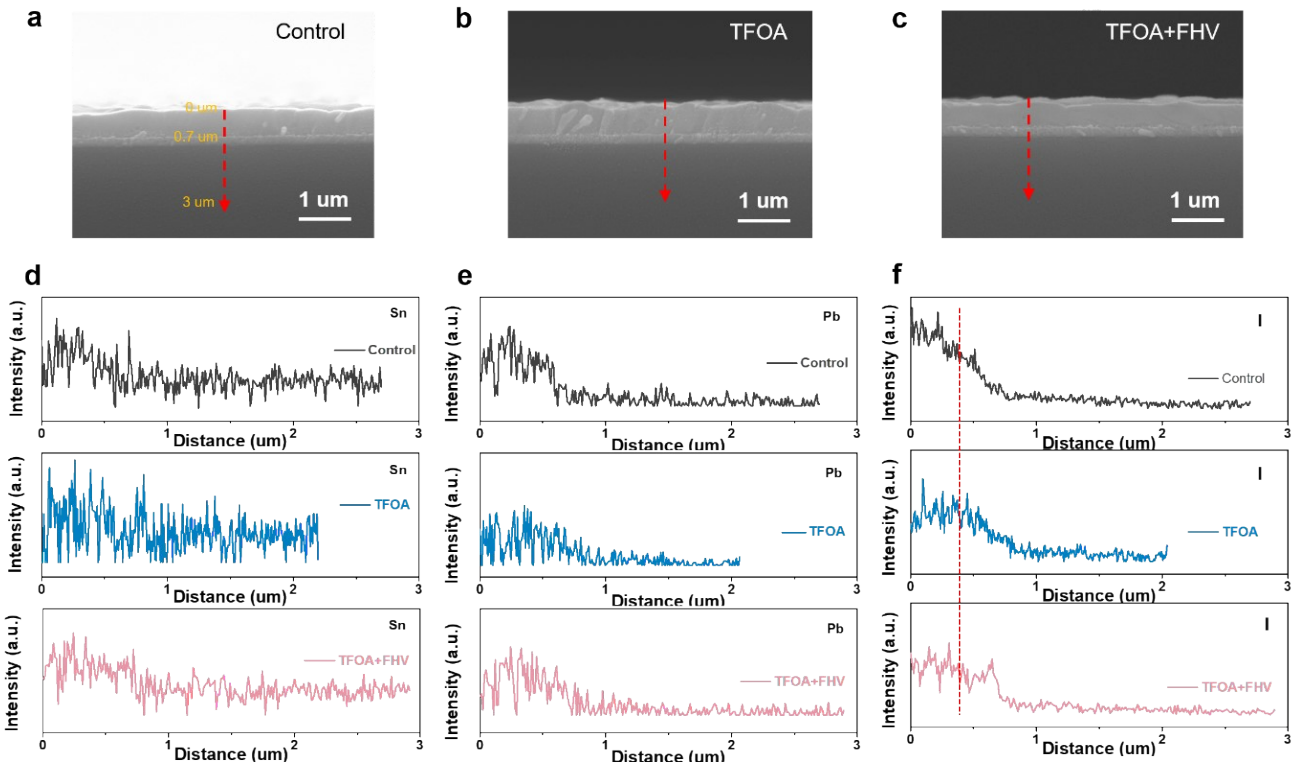

Fig. S17 EDS line scans from top to bottom across the three conditional perovskite films for (a) the control, (b) TFOA-only and (c) TFOA-FHV based. EDS signal distribution of (d) Sn element, (e) Pb element and (f) I element.

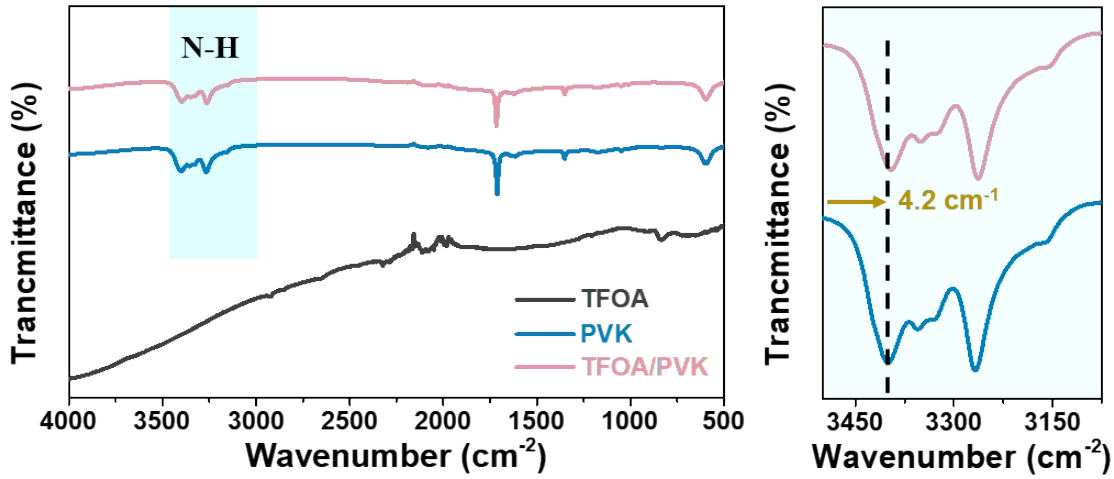

Fig. S18 FT-IR spectra of TFOA, PVK and TFOA/PVK, the right view shows an enlarged image of FT-IR spectra in the range of 3000-3500 cm^{-1}.

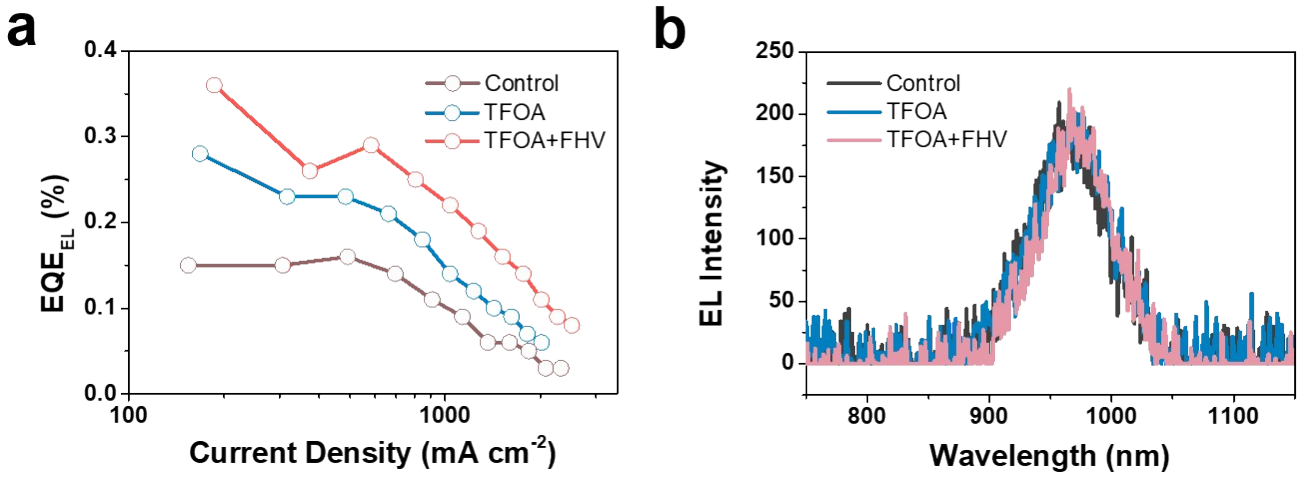

Fig. S19 (a) EQE_{EL} values and (b) EL intensity at 1.2 V voltage.

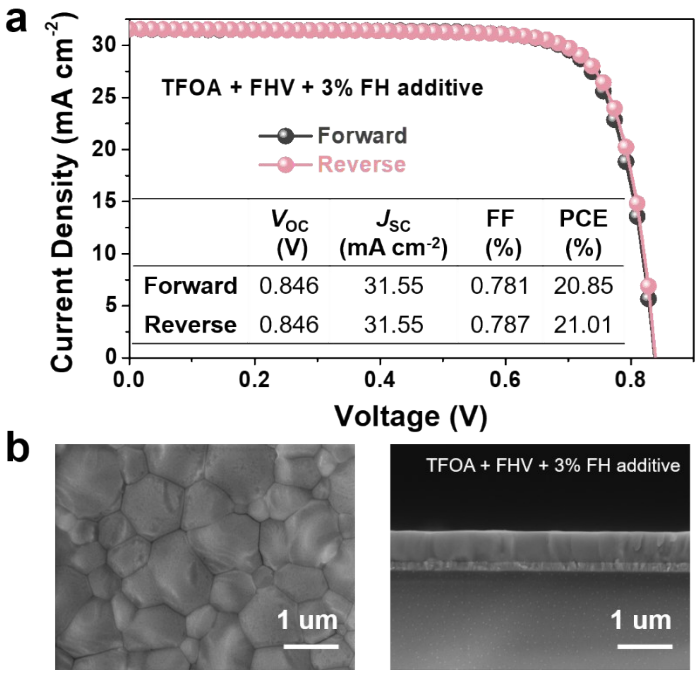

Fig. S20 (a) The *J-V* curves of the champion device for TFOA+FHV+3% FH additive based devices under both the reverse (pink) and forward (black) scan directions. (b) The surface (left) and corresponding cross-section (right) SEM images of TFOA+FHV+3% FH additive co-modified perovskite films.

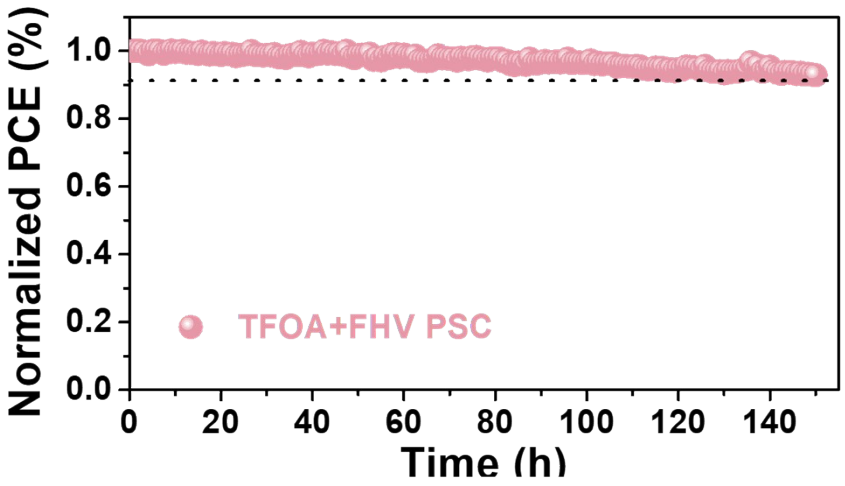

Fig. S21 The MPP tracking of encapsulated solar cells under continuous white light illumination (100 mW cm^{-2}) in the atmospheric environment (relative humidity ≈ 25%).

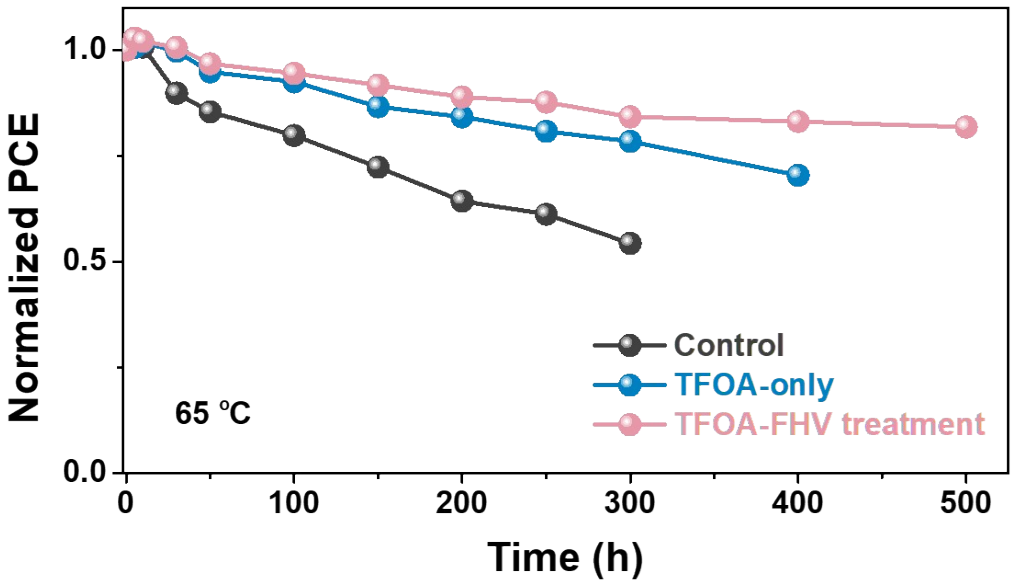

Fig. S22 Thermal stability at 65°C of three conditional devices for the control, TFOA-only and TFOA-FHV based.

Table S1. Parameters of TAS of perovskite based on bare NiO_x and NiO_x/TFOA substrates.

Samples	**A_1**	***τ_1 (ps)***	**A_2**	***τ_2 (ps)***	***τ_{ave} (ps)***
NiO_x-$FAPb_{0.5}Sn_{0.5}I_3$	0.273	49.042	0.584	1020.288	998.96
NiO_x-TFOA-$FAPb_{0.5}Sn_{0.5}I_3$	0.431	390.666	0.388	18.922	375.14

Table S2. Parameters of TRPL of TFOA modified perovskite with or without FHV treatment on glass substrates.

Samples	**A_1**	***τ_1 (ns)***	**A_2**	***τ_2 (ns)***	***τ_{ave} (ns)***
TFOA-$FAPb_{0.5}Sn_{0.5}I_3$	17.15956	2.79431	0.27726	308.47891	89.96
TFOA-FHV-$FAPb_{0.5}Sn_{0.5}I_3$	0.27193	515.81317	91.78238	1.99426	224.91

Table S3. Photovoltaic parameters of the champion devices of the control, TFOA-only modified and TFOA-FHV based.

		PCE (%)	**V_{OC} (V)**	**J_{SC} (mA cm^{-2})**	**FF (%)**
Control	Forward	16.26	0.756	29.63	72.6
	Reverse	16.28	0.756	29.63	72.7
TFOA	Forward	19.82	0.822	31.29	77.2
	Reverse	20.11	0.836	31.29	76.9
TFOA-FHV	Forward	20.99	0.846	31.39	79.1
	Reverse	21.12	0.846	31.39	79.5

Table S4. The V_{TFL} values and the trap density values (calculated from *SCLC*) of the control, TFOA-only modified and TFOA-FHV based devices.

Sample	**V_{TFL} (V)**	**Trap density (cm^{-3})**
Control	0.67	$7.31*10^{15}$
TFOA	0.43	$4.69*10^{15}$
TFOA-FHV	0.34	$3.71*10^{15}$

Table S5. Summary of FA-dominant (FA≥85%) Sn-Pb binary perovskite solar cells in recent five years.

Perovskite component	V_{OC} (V)	J_{SC} (mA cm^{-2})	FF (%)	PCE (%)	Ref.
$FAPb_{0.5}Sn_{0.5}I_3$	0.75	19.48	70.3	10.27	5
$FAPb_{0.5}Sn_{0.5}I_3$	0.695	28.37	54.6	10.76	6
$FAPb_{0.75}Sn_{0.25}I_3$	0.81	28.23	75.4	17.25	7
$FAPb_{0.5}Sn_{0.5}I_3$	0.782	28.51	73.0	16.27	8
$FAPb_{0.7}Sn_{0.3}I_3$	0.778	26.46	79.0	16.26	9
$FA_{0.85}MA_{0.15}Pb_{0.6}Sn_{0.4}I_{2.55}Br_{0.45}$	0.87	26.45	79.1	18.21	10
$FAPb_{0.5}Sn_{0.5}I_3$	0.69	26.56	73.0	13.33	11
$FAPb_{0.5}Sn_{0.5}I_3$	0.72	24.5	79.3	13.98	12
$FA_{0.85}MA_{0.1}Cs_{0.05}Pb_{0.5}Sn_{0.5}I_3$	0.865	29.81	79.1	20.4	13
$FA_{0.9}Cs_{0.1}Pb_{0.7}Sn_{0.3}I_3$	0.804	29.4	81.8	20.0	14
$FAPb_{0.5}Sn_{0.5}I_3$	0.69	20.99	67	9.77	15
$FA_{0.85}Cs_{0.15}Pb_{0.5}Sn_{0.5}I_3$	0.76	31.3	73	17.4	16
$FAPb_{0.5}Sn_{0.5}I_3$	0.841	31.7	78.9	21.0	17
$FAPb_{0.5}Sn_{0.5}I_3$	0.846	31.09	78	20.53	1

$FAPb_{0.5}Sn_{0.5}I_3$	0.828	30.88	76.2	19.48	18
$FAPb_{0.5}Sn_{0.5}I_3$	0.846	31.39	79.5	21.12	**This work**

Supplementary references

1. Y. Zhou, Z. Wang, J. Jin, X. Zhang, J. Zou, F. Yao, Z. Zhu, X. Cui, D. Zhang, Y. Yu, C. Chen, D. Zhao, Q. Cao, Q. Lin and Q. Tai, *Angew. Chem. Int. Ed.*, 2023, **135**, e202300759.
2. M. J. Frisch, G. W. Trucks, H. B. Schlegel, et al., Gaussian 16 Revision. A.03, Gaussian Inc., Wallingford, CT, 2016.
3. W. Humphrey, A. Dalke and K. Schulten, VMD: Visual molecular dynamics. *J Mol Graph Model*, 1996, **14**, 33-38.
4. S. Hu, K. Otsuka, R. Murdey, N. Tomoya, A-T. Minh, Y. Takumi, H. Taketo, M. Kazuhiro, N. Kyohei, S. Atsushi, M. Kazuhiro, T. Keisuke, K. Yoshihiko, W. Atsushi, *Energy Environ. Sci.* 2022, **15**, 2096-2107.
5. X. Liu, Z. Yang, C.-C. Chueh, A. Rajagopal, S. T. Williams, Y. Sun and A. K.-Y. Jen, *J. Mater. Chem. A*, 2016, **4**, 17939-17945.
6. J. Liu, G. Wang, Z. Song, X. He, K. Luo, Q. Ye, C. Liao and J. Mei, *J. Mater. Chem. A*, 2017, **5**, 9097-9106.
7. D. Chi, S. Huang, M. Zhang, S. Mu, Y. Zhao, Y. Chen and J. You, *Adv. Funct. Mater*., 2018, **28**, 1804603.
8. S. Shao, Y. Cui, H. Duim, X. Qiu, J. Dong, G. H. Ten Brink, G. Portale, R. C. Chiechi, S. Zhang, J. Hou and M. A. Loi, *Adv. Mater.*, 2018, **30**, 1803703.
9. X. Lian, J. Chen, Y. Zhang, M. Qin, J. Li, S. Tian, W. Yang, X. Lu, G. Wu and H. Chen, *Adv. Funct. Mater*., 2019, **29**, 1807024.
10. Z. Zhu, N. Li, D. Zhao, L. Wang and A. K. Y. Jen, *Adv. Energy Mater.*, 2019, **9**, 1802774.
11. C. Park, J. Choi, J. Min and K. Cho, *Acs Energy Lett.*, 2020, **5**, 3285-3294.
12. A. M. Igual-Muñoz, J. Ávila, P. P. Boix and H. J. Bolink, *Sol. RRL*, 2020, **4**, 1900283.
13. C. Li, Z. Song, C. Chen, C. Xiao, B. Subedi, S. P. Harvey, N. Shrestha, K. K. Subedi, L. Chen, D. Liu, Y. Li, Y.-W. Kim, C.-S. Jiang, M. J. Heben, D. Zhao, R. J. Ellingson, N. J. Podraza, M. Al-Jassim and Y. Yan, *Nat. Energy.*, 2020, **5**, 768-776.
14. J. Tong, J. Gong, M. Hu, S. K. Yadavalli, Z. Dai, F. Zhang, C. Xiao, J. Hao, M. Yang, M. A. Anderson, E. L. Ratcliff, J. J. Berry, N. P. Padture, Y. Zhou and K. Zhu, *Matter*, 2021, **4**, 1365-1376.
15. J. Xi, H. Duim, M. Pitaro, K. Gahlot, J. Dong, G. Portale and M. A. Loi, *Adv. Funct. Mater.*, 2021, **31**, 2105734.

16. H. Liu, J. Sun, H. Hu, Y. Li, B. Hu, B. Xu and W. C. Choy, *ACS Appl. Mater. Interfaces*, 2021, **13**, 45059-45067.
17. P. Wu, J. Wen, Y. Wang, Z. Liu, R. Lin, H. Li, H. Luo and H. Tan, *Adv. Energy Mater.*, 2022, **12**, 2202948.
18. H. Zhang, Y. Zhou, T. Guo, X. Zhang, Z. Zhu, J. Jin, X. Cui, D. Zhang, Z. Wang, L. Li, N. Wang, G. Tang and Q. Tai, *Chinese J. Chem.*, 2023, **41**, 3197-3204.